This is a post-print. The Online version is found via. AIAA J. website:
https://arc.aiaa.org/doi/full/10.2514/1.J057615
where supplementary animation can also be downloaded.

The near-wake of an inclined 6:1 spheroid at Reynolds number 4000

Håkon Strandenes[1], Fengjian Jiang[1], Bjørnar Pettersen[1], and Helge I. Andersson[2]
[1]*Department of Marine Technology,*
[2]*Department of Energy and Process Engineering*
[1,2]*Norwegian University of Science and Technology, NO-7491 Trondheim, Norway*
Corresponding author e-mail: `fengjian.jiang@ntnu.no`

We describe the flow around a 6:1 prolate spheroid at 45° inclination angle and Reynolds number 4000 based on the minor axis. Despite that the inflow is uniform and steady, the resulting wake is highly asymmetric and unsteady. Two main vortical structures develop from the shear layers of the spheroid, one being significantly stronger than the other. This asymmetry results in a non-zero sideforce. The forces acting on the spheroid change dramatically from earlier works at Reynolds number 3000. The pressure inside the vortex cores also changed with this moderate increase in Reynolds number. This indicates that the flow is highly transitional. We also document that close to the body, on the side of the weaker vortex, there is a region of negative axial velocity. In this backflow region, the fluid enters from behind the spheroid and travels forward against the inflow and then exits the backflow region through one of the main vortical structures. This backflow has not been described before. We also observe and describe a distinct Kelvin-Helmholtz shear layer instability close to this region.

Nomenclature

λ	Aspect ratio $\lambda = L : D$	F_i	Force on spheroid, $i \in (x, y, z)$
λ_2	Vortex identification measure	f	Frequency
ν	Kinematic viscosity of fluid	L	Spheroid length
ρ	Density of fluid	M_i	Torque on spheroid around the axis i, $i \in (x, y, z)$
ω	Vorticity	p	Instantaneous pressure
A_{ref}	Reference area	$\overline{p}$	Time-averaged pressure
C_{Fi}	Force coefficient, $i \in (x, y, z)$	Re_D	Reynolds number $Re = DU_\infty/\nu$
C_{Mi}	Torque coefficient, $i \in (x, y, z)$	u, v, w	Instantaneous fluid velocity
C_p	Pressure coefficient	U_∞	Inlet (freestream) velocity
D	Spheroid diameter	x_{ax}	Spheroid major axis
d	Reference length $d = 1.817D$	x, y, z	Cartesian coordinates

I. Introduction

The 6:1 prolate spheroid serves as a model for various objects ranging from particles suspended in a fluid; underwater vehicles or submarines in the ocean to aircraft, rockets and drones in the air. Different aspect ratios and attack angles, give rise to a wide range of interesting flow features such as 3-D flow separation, wake asymmetry, etc. Therefore, laboratory experiments and numerical simulations of the flow around a prolate spheroid and its wake have become an appealing research topic for flow physicists and engineers. The intrinsic complexity of the flow physics in the wake also makes it an interesting case for high-resolution flow simulations (Direct Numerical Simulations - DNS).

The prolate spheroid geometry has been used to study boundary layer separation, see e.g. Wang [1] and Geissler [2]. Flow separation experiments are reported by Wetzel et al. [3]. Later on, more complicated experiments with 3-D flow measurements took place [4]. Due to the similarity with various vehicles, the prolate spheroid has also been used as prototype in manoeuvring experiments (e.g. Rhee and Hino [5]). The full history on this topic is properly summarized in Simpson [6] and Andersson et al. [7], therefore it will not be repeated here. Nevertheless, it is important to notice that in early research works, emphasis was on the integral body forces and flow details close to the geometry (essentially surface flow, boundary layers, separation, or in special cases the very near wake). Difficulties in measuring the complex wake in an experiment, the use of simplified numerical methods, as well as limited computational power, have all been constraints in earlier studies of the wake field behind a prolate spheroid. This is to a certain degree still the case.

DNS, however, is able to produce reliable and detailed results of the 3-D flow fields, and in-depth investigations of the complex wake is possible from the simulation data. DNS studies of the prolate spheroid wake were carried out by El Khoury et al. [8, 9], in which they described the detailed wake flow behind a 6:1 prolate spheroid in cross-flow, and outlined the special flow features and the wake transition scenario for this configuration. The wake of the prolate spheroid in cross-flow contains geometrical features similar to both finite-length cylinder wakes and wakes behind spheres, but turns out to be different from both.

The wake behind a 6:1 prolate spheroid, but at angle of attack 45°, were systematically investigated by Jiang et al. [10–12]. A wide range of Reynolds numbers (Re_D, defined based on the minor axis D) from 50 to 3000 were considered. These studies reveal that the dominating structure of the laminar wake when $Re_D < 1000$ is a pair of counter-rotating vortices. These vortices originate from the shear layers separated from the two sides of the spheroid, starting at the tip of the spheroid while growing larger downstream. This steady and fully symmetric laminar wake persists to a relatively high $Re_D = 1000$, at which the primary instability was observed, and the wake partly looses its symmetry (in the far wake only). At Reynolds numbers higher than about 1000, the wake becomes unsteady and asymmetric, but no vortex shedding or vortex filament flapping could be observed in the wake. As a result, the time-averaged flow field is also heavily asymmetric, thus exerts a strong side force onto the geometry.

The asymmetric time-averaged flow fields, together with the strong side force, deliver an important message. People have only considered this kind of asymmetric wake for sharp-nosed slender bodies such as a air-fighter forebody

[13, 14], and assumed that this asymmetry would not occur with blunt-nosed bodies, because they are generally less sensitive to asymmetric disturbances [15]. Coincidentally, a similar side force and asymmetric wake were observed in an experimental study carried out by Ashok et al. [16], for a spheroid-like submarine hull at incidence. These results revealed, beyond any doubt, that asymmetry is an intrinsic feature of similar wake flows. This conclusion may be especially important for the marine and aerospace community because prolate spheroids can be an idealized prototype for UUVs (Unmanned Underwater Vehicles), submarine bare hulls, and various aircraft, and the asymmetric wake may have significant influence on the manoeuvring capabilities of these vehicles.

Jiang et al. [17] continued their investigations of the 45°-inclined prolate spheroid wake, and conducted more detailed explorations of the coherent structures in the wake, i.e. a concentrated helical vortex, at $Re_D = 3000$. They took advantage of the very detailed flow information from a DNS simulation, and reported several interesting features of the coherent wake structure and complex vortex interactions in this specific wake problem.

Encouraged by the recent progress, we aim to further increase the Reynolds number of the 45°-inclined 6:1 prolate spheroid to $Re_D = 4000$, and study the flow physics in the resulting near-wake. We have learned from previous studies that the wake is transitional at $Re_D = 3000$. Therefore, a modest increase in Re_D has two advantages: firstly, the main features of the wake should not change dramatically; secondly, since the wake is under transition, we might anticipate new and interesting flow features. Although this range of Reynolds numbers is outside the operating conditions of the type of vehicles mentioned earlier, this Reynolds number regime is ideal for simulations both in order to describe and understand fundamental flow physics and to serve as computational benchmarks and validation for large eddy simulations (LES), detached eddy simulations (DES) and Reynolds-averaged Navier-Stokes (RANS) simulations.

II. Problem and definitions

This paper presents the flow around a prolate spheroid with an aspect ratio of $\lambda = L : D = 6 : 1$, where L is the length of the major axis and D is the length of the two minor axes. D is thus also the maximum diameter of the circular cross-section that appears when the spheroid is sliced perpendicular to the major axis. The spheroid's orientation in the global coordinate system is found by first aligning the major axis of the spheroid x_{ax} with the global x-axis, and then rotating it 45° around the global z-axis. The constant inflow velocity is uniform $u = U_\infty$ in the positive x-direction with $v = w = 0$. The outlet is a fixed-pressure boundary condition with zero-gradient Neumann conditions for the velocity. The four other side boundaries (perpendicular to the y and z-axes) of the domain are slip-walls in which the wall-normal velocity component is prescribed to be zero, while the two other velocity components and the pressure have a zero-gradient Neumann condition. The flow is incompressible and assumed to be governed by the Navier-Stokes equations together with the equation for conservation of mass. The Reynolds number based on the equatorial diameter D is $Re_D = DU_\infty/\nu = 4000$ in the present work.

The size of the computational domain is shown in figure 1. To facilitate easy discussion we choose to adopt the

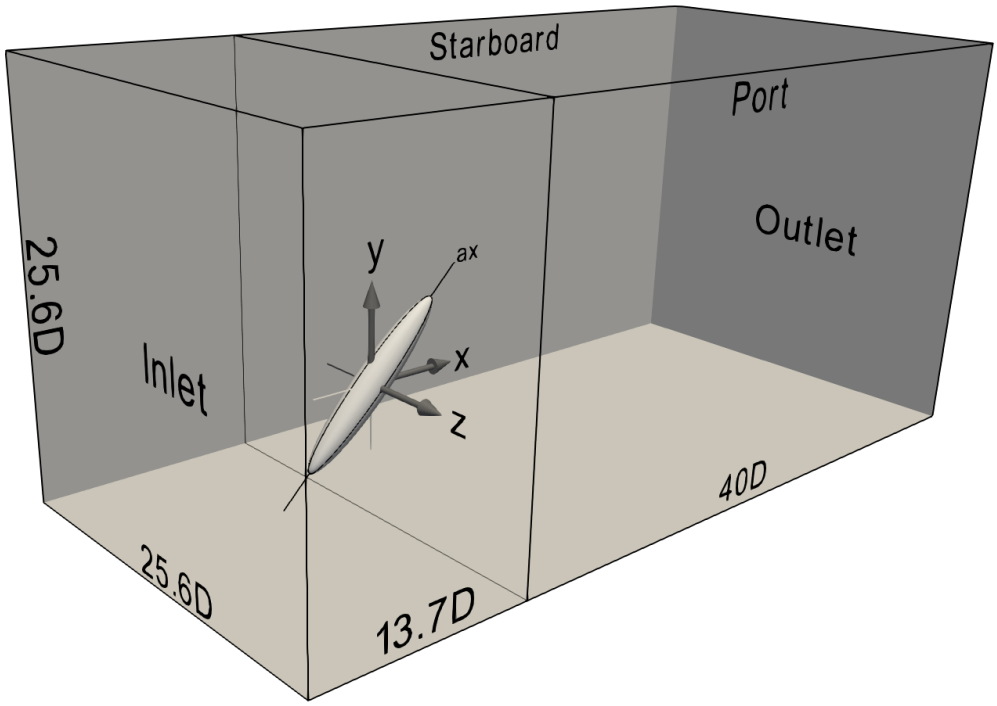

Figure 1 Computational domain and coordinate systems. D is the length of the spheroid's minor axis. The origin of the coordinate systems is in the center of the spheroid. To emphasize the spheroid shape and orientation, it is enlarged with respect to the surrounding domain. The terms *starboard* and *port* are used for the sides corresponding to the negative and positive z-axis, respectively. The spheroid is pointing with its nose down.

(aero)nautical terms *port* and *starboard* to distinguish the two sides of the spheroid. The port side is to the left when the observer is positioned at the spheroid and looking against the oncoming flow. In mathematical notation, the port side is the half of the spheroid with $z > 0$ and the starboard side is the half of the spheroid with $z < 0$.

We will also use a rotated coordinate system to present results. This coordinate system is found by rotating the original coordinate system (in which the inflow is parallel to the x-axis) 45° in positive direction around the z-axis, such that the resulting first axis coincide with the major axis of the spheroid. Flow variables presented in the rotated coordinate system will have the 'ax'-subscript, e.g. the flow velocity u_{ax}.

To enhance the 3-D visualizations and help in setting the point of view, we have added two meridian lines to several of the figures presented in this paper. The first line is the intersection line between the spheroid and the xy-plane, and the second line is the intersection between the spheroid and the zx_{ax}-plane.

III. Numerical methods

The code *MGLET* [18] has been used to perform all simulations presented in this paper. MGLET uses a finite-volume formulation on staggered Cartesian grids to solve the incompressible Navier-Stokes equations using linear interpolation and integration for all spatial terms, hence leading to second-order accuracy in space. A third-order low-storage explicit

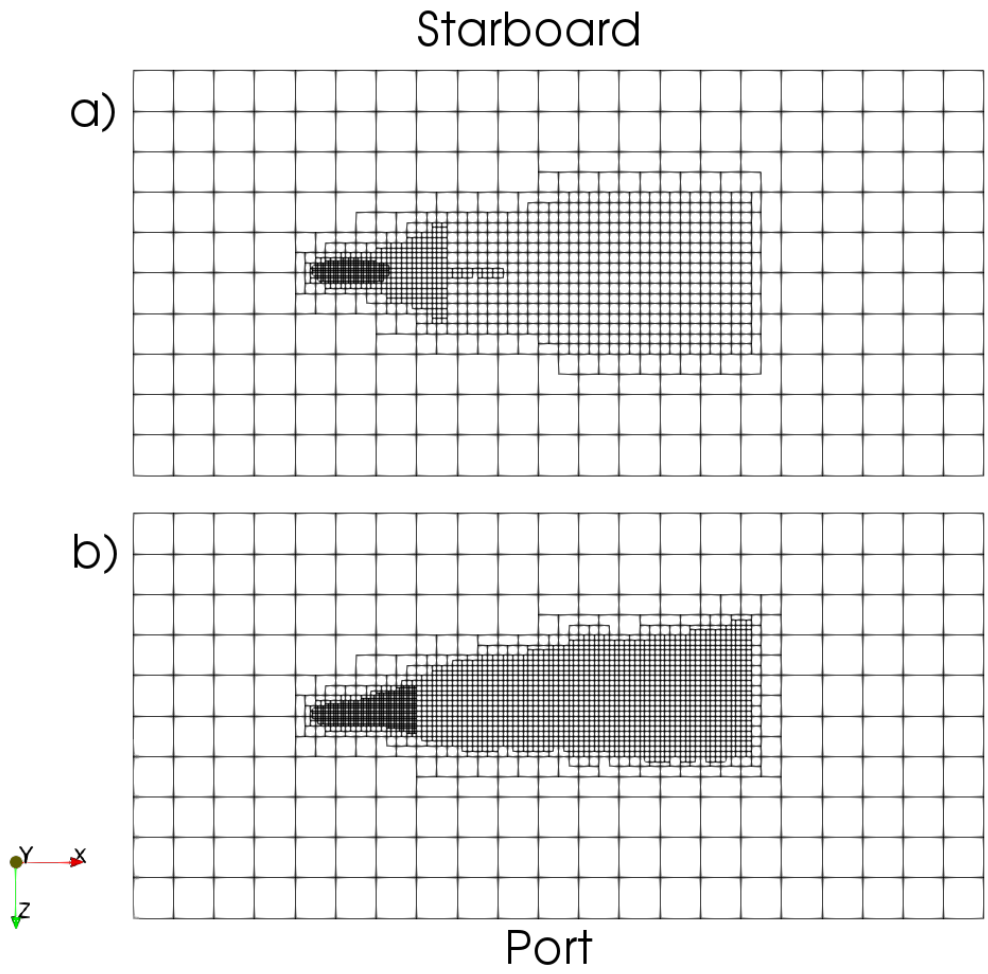

Figure 2 a) grid on which initial development of flow was conducted b) final grid on which the final results are computed. Each box in the figure represents a cube of $40 \times 40 \times 40$ grid cells.

Runge-Kutta time integration scheme [19] is used for time stepping. The time step is fixed at 0.001 D/U_∞ in the entire simulation.

MGLET introduces the solid geometry through an immersed boundary method [20]. A local refinement of the grid around the spheroid is achieved by constructing a multi-grid hierarchy that together form an unstructured arrangement of Cartesian grid boxes. In the simulation presented here, we use five grid levels in total. This resolves the solid geometry surface, its boundary layers and the wake behind it sufficiently while keeping the total number of grid cells at a reasonable level. The refinement process is a simple cell splitting, in which each parent grid cell subject to refinement is split into eight equal (3-D) child cells [21].

To develop an efficient grid without wasting cells in areas with no interesting flow structures, we initially constructed a symmetric grid with the desired final resolution close to the spheroid surface, as seen in figure 2a). The flow was simulated on this grid for a long time, and when the asymmetry was fully developed, we mapped the flow on to a new,

Table 1 Grid and simulation parameters compared to reference [11]. $\Delta x, \Delta y, \Delta z$ **is the grid spacing.**

Case	$Re_D = 3000$ [11]	$Re_D = 4000$ (present)
$min(\Delta x, \Delta y, \Delta z)$	$0.006D$	$0.004D$
Number of grid cells	0.75×10^9	2.1×10^9
Time step	$0.001D/U_\infty$	$0.001D/U_\infty$
Sampling time	$600D/U_\infty$	$369D/U_\infty$
Domain size $L_x \times L_y \times L_z$	$38D \times 24D \times 21D$	$53.7D \times 25.6D \times 25.6D$

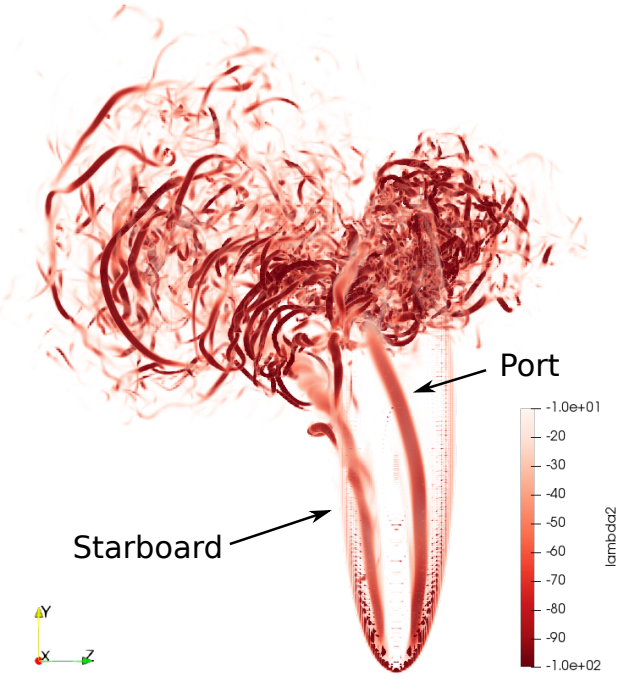

Figure 3 3-D Rendering of the λ_2 vortex identification criterion [22], seen seen from upstream. The spheroid body is not shown, to be able to see the flow structures behind it. The figure is created at time $t = 345.760D/U_\infty$.

asymmetric grid with improved wake resolution, as shown in figure 2b). After a second, short, simulation we used this result as the initial condition for all further simulations from where our reference time sampling $t = 0$ starts.

The resulting grid and simulation parameters are summarised in table 1. It is worth mentioning that due to recent efficiency improvements in the MGLET code, the present simulations are considerably cheaper to execute compared to previous works, despite the fact that we have nearly three times as many grid cells as in [11].

IV. Results

A. Forces and torques

Similar to Reynolds number 3000 [11], the present wake is highly asymmetric, see figure 3. Because of this, there is a strong sideforce F_z acting on the spheroid. The average sideforce is of the same order of magnitude as the average

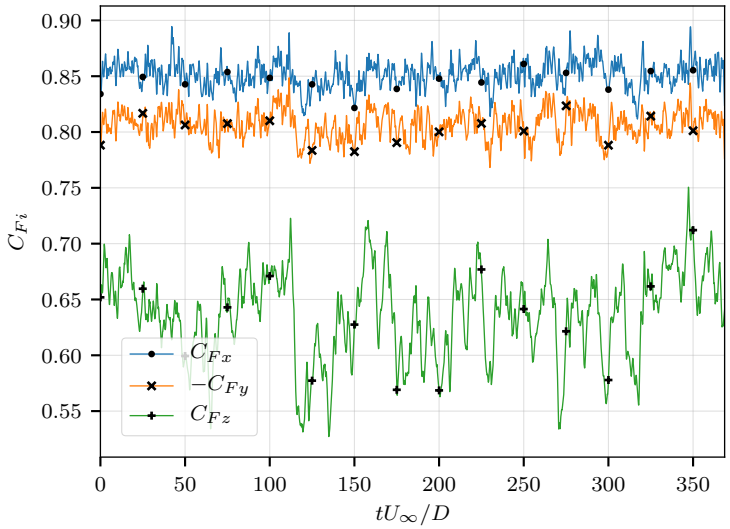

Figure 4 Force coefficients on the spheroid during the simulation.

Table 2 Mean and root-mean-square (RMS) of the force and torque coefficients. Coefficients at $Re_D = 3000$ are from [11].

Re_D		C_{Fx}	C_{Fy}	C_{Fz}	C_{Mx}	C_{My}	C_{Mz}
3000 (ref [11])	Mean	0.879	-0.796	-0.645	-0.168	0.166	0.311
	RMS	0.006	0.006	0.019	0.009	0.009	0.010
4000 (present)	Mean	0.852	-0.807	0.637	0.084	-0.082	0.315
	RMS	0.012	0.013	0.039	0.019	0.019	0.015

drag force F_x. See figure 4. Since the inflow and geometry is symmetric about the xy-plane, this asymmetry is caused by the resulting flow only.

In this work we normalize all forces the same way

$$C_{Fi} = \frac{F_i}{\frac{1}{2}\rho U_\infty^2 A_{\text{ref}}} \quad , \quad i = x, y, z \tag{1}$$

and for the torques

$$C_{Mi} = \frac{M_i}{\frac{1}{2}\rho U_\infty^2 A_{\text{ref}} d} \quad , \quad i = x, y, z \tag{2}$$

where M_i is the torque around axis i in the coordinate system given in figure 1. The reference length $d = 1.817D$ is the diameter of a sphere with the same volume as the 6:1 spheroid, and the reference area is $A_{\text{ref}} = \pi d^2/4$. This is the same as used in previous literature on the same geometry.

Table 2 gives the force coefficients for each of the three main directions. We see that in the present case, both the drag (C_{Fx}) and the sideforce (C_{Fz}) are slightly lower in magnitude than the corresponding values for $Re_D = 3000$ [11]. The average drag coefficient is $C_{Fx} = 0.852$ in our case, and the average sideforce coefficient is $C_{Fz} = 0.637$, that is 75 % of the magnitude of the drag force. Since the wake developed to the other side in the $Re_D = 3000$ case, the sideforce C_{Fz} and torques C_{Mx} and C_{My} have the opposite sign in the two cases. The different wake asymmetry is caused by insignificant numerical differences in the initial development of the flow. Each of the two asymmetric wakes are equally likely. The vertical lift force is $C_{Fy} = -0.807$, approximately the same as in the $Re_D = 3000$ case.

For $Re_D = 3000$ Jiang et al. [11] observed clear periodic oscillations in the sideforce F_z with a period of around $13.6D/U_\infty$, see figure 2 in [11]. At the present Reynolds number, the sideforce coefficient history, as shown in figure 4, no longer show any obvious periodic patterns. However, the magnitude of the fluctuations are twice as large, as seen in the difference in the RMS of C_{Fz} between the cases.

Compared to the previously reported force coefficients at $Re_D = 3000$, table 2 shows much of the same general tendency, except for the torque coefficients C_{Mx} and C_{My}. At the Reynolds number of 4000, the magnitude of the mean torque around the x and y-axis is half of that at Reynolds number 3000, but the root-mean-square (RMS) value of the fluctuations of the two coefficients are twice as large. At the present Reynolds number the RMS of the torque coefficients C_{Mx} and C_{My} are now about 25 % of the mean value. Similarly, the RMS of the force coefficients in all three directions have doubled. One possible explanation can be that this is a consequence of the increased turbulence and chaos in the flow associated with the strong port side vortex. The turbulence provides a more uniform and symmetric loading in average, but the oscillations are much higher in this more turbulent flow regime compared to $Re_D = 3000$.

The pressure in the core of the two main vortices are of interest to study. Jiang et al. [17] presented the pressure along the core of the weaker vortex (in the present case this is the starboard vortex in figure 3), which showed two

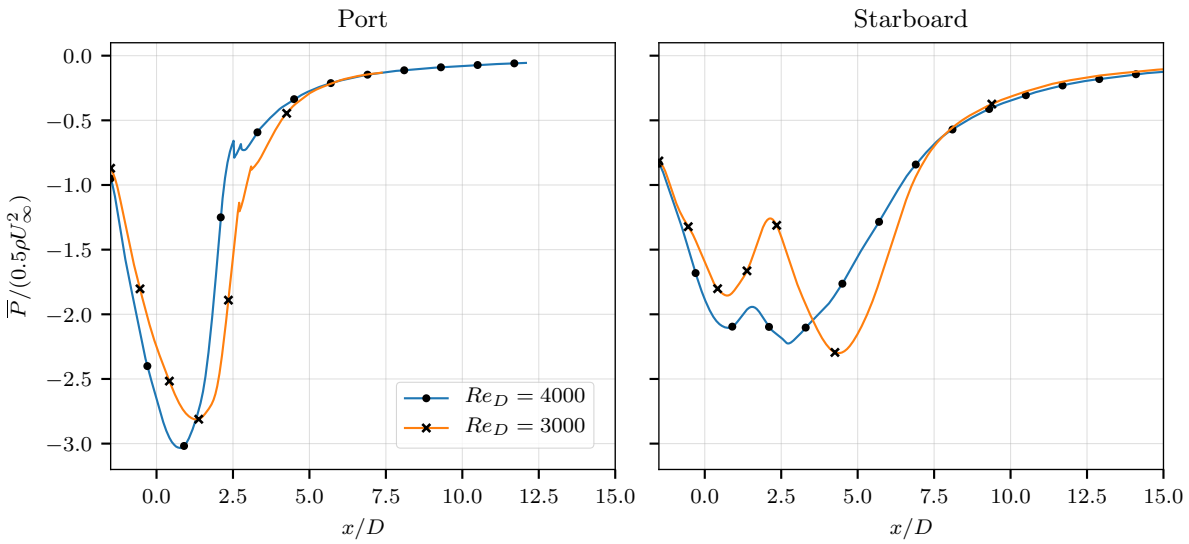

Figure 5 Time-average of pressure in the vortex cores of the present case compared to Reynolds number 3000. The Reynolds number 3000 results are mirrored (i.e. port and starboard are switched) to be comparable with the present case. Results from $Re_D = 3000$ are from [17].

distinct minima. In the present $Re_D = 4000$ case, we extracted the pressure along both vortex cores (defined as the locus of the pressure minima) in the same way, and observe a striking difference in both the strong and weak vortex. This is shown in figure 5. The present strong port side vortex have grown even stronger (with lower pressure), and the location of the pressure minima have shifted forwards slightly. In the weaker vortex core there were previously two distinct pressure minima with a significant peak in between. This was associated with the helical vortex alteration as described by [17]. These minima have now shifted both in magnitude and position, and are now nearly joined, only separated with a slight increase in pressure. The maxima in between them also has a much lower pressure. The fact that the increase in Reynolds number between the cases is very modest, supports the claim that the present case is highly transitional and only a small change in Reynolds number gives rise to huge changes in the flow structures.

B. Overall wake topology

The coherent vortical structure originating from the weak starboard tip vortex is still present as for the lower Reynolds numbers, but it now appears to be more unsteady. Starting from the tip of the spheroid, a counter-rotating vortex pair is generated from the shear layers, see plane at $x/D = -1.5$ in figure 6. In the front part at $x/D = -1.5$, the port side vortex grows stronger by 25 % compared to the starboard side vortex, creating an imbalance between the two. The result is that the vortices twist and bend such that the stronger, port vortex is attracted to the spheroid surface, moving towards the centerline further downstream along the spheroid, and the weaker starboard vortex is deflected outwards and downwards from the spheroid surface, see figure 6. The stronger port vortex is not much affected, neither by the shear layers forming from the spheroid nor the freestream, because it is mostly sheltered behind the spheroid body. Hence it is

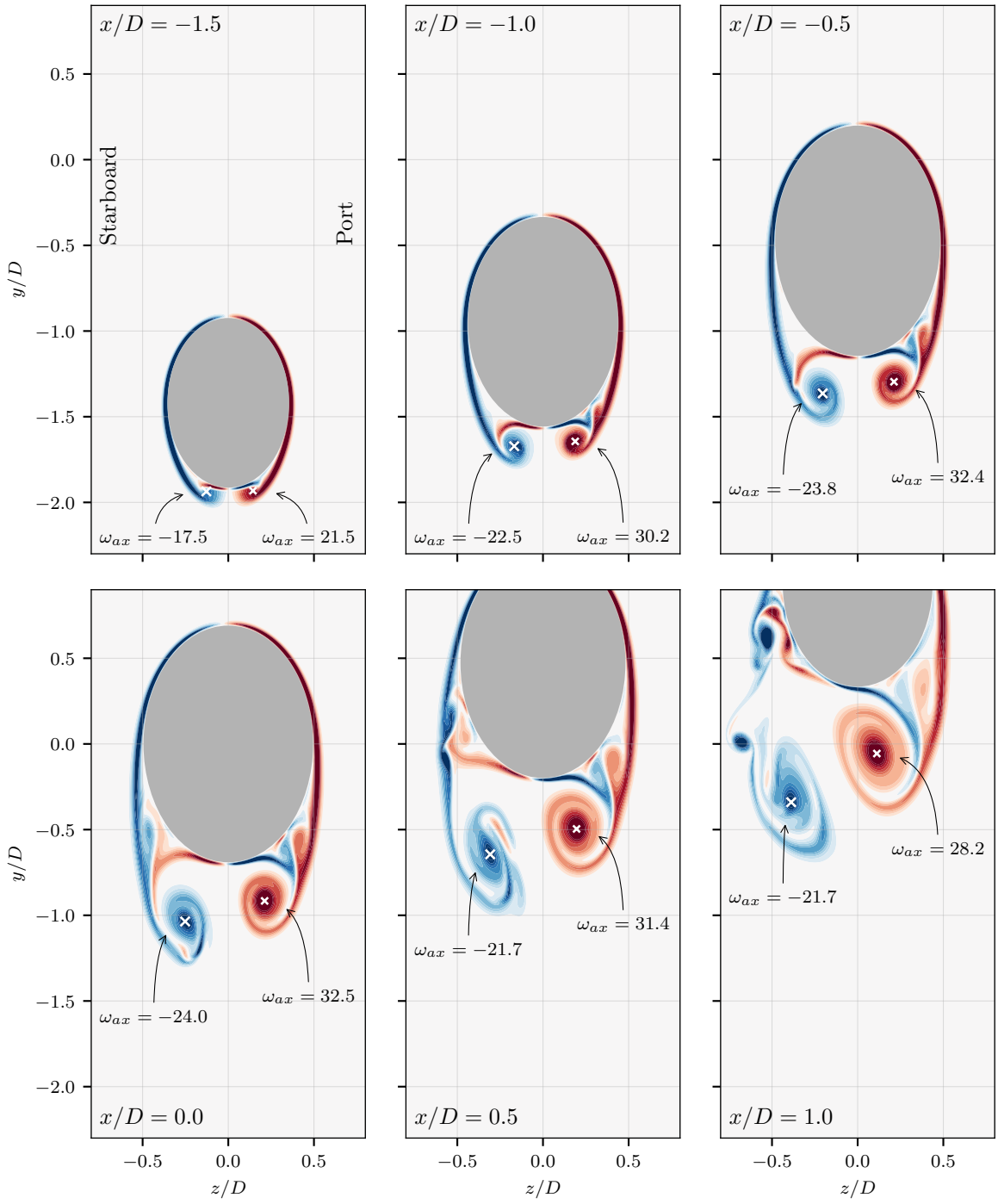

Figure 6 Axial vorticity ω_{ax} in six yz-planes along the spheroid, indicating the development of the tip vortices. Figures are created at time $t = 345.760D/U_\infty$. The maxima and minima of ω_{ax} in the vortex cores are indicated with a white cross. Blue colors indicate negative and red colors indicate positive vorticity. All individual plots share the same color scales.

nearly stationary. However, when the stronger port vortex reaches the aft end of the spheroid, close to $x/D = 2.0$, and meets the flow coming over the spheroid, it immediately disintegrates into smaller turbulent structures. The weaker starboard vortex on the other hand, interacts with both the shear layers forming from the sides of the spheroid and the freestream, but in a highly complicated manner.

C. Axial flow behind the spheroid

There is a strong axial flow underneath the spheroid, see figure 7. The maximum value of the axial velocity u_{ax} exceeds 1.5 times the freestream velocity. This was first reported and described by Jiang et al. [11]. Very close to the nose of the spheroid (around $x/D = -1.5$), the axial flow is strongest *between* the port and starboard vortex, and further downstream the axial flow in both vortex cores increases in strength and exceeds the velocity between the vortices. The strong port vortex provides a stronger axial flow field than the weaker starboard vortex. This is similar to the results at $Re_D = 3000$ [11] and will not be discussed any further in this paper.

In the present simulation we observe a region of moderately strong *negative* axial velocity ($u_{\mathrm{ax}} < 0$) on the starboard side of the spheroid, see figure 7 and 8. The region of negative axial velocity is at the same side as the weaker vortex. The negative axial velocity also leads to the formation of not only one, but two distinct shear layers with different direction of the shear. The first shear layer is between the spheroid surface (with $u = v = w = 0$) and the region of negative axial velocity, and the second shear layer is between this region and the freestream. These shear layers are easily visible as thin white layers in figure 7.

To investigate details in the region of negative axial velocity, we randomly selected a number of seedpoints in the volume where $u_{\mathrm{ax}} < 0$. From these points we integrated streamlines in the instantaneous velocity field both downstream and upstream. The result is shown in figure 8. We notice that a large majority of the fluid particles that end up in the region of negative axial velocity, originate from the port side of the spheroid nose. After the fluid particles 'turn around' underneath the nose, from the port to the starboard side, they are captured by the powerful upwards axial flow that is established between the two main vortices. The main wake deflects towards starboard in this case, and so do the fluid particles. When they reach about halfway up along the spheroid, the fluid particles change direction and travel towards the spheroid nose again. Eventually they are captured by the starboard vortex and escape, repelled downstream in the helical vortex core. From this we understand that the region of negative axial velocity is *not* a *recirculation region* where the same fluid is constrained in a small region and circulate without exchange of fluid, but a *backflow* region where the fluid enter in the rear part, flows towards the nose of the spheroid, and leaves through the starboard vortex. 'Fresh' fluid continuously enters and leaves the backflow region.

The exact mechanisms creating this backflow region is not yet fully understood, however, we suspect that differences in separation patterns between port and starboard side of the spheroid have strong influence on it. On the port side, there is suction due to the strong vortex (which is the cause of the strong sideforce F_z), while on the starboard side there is

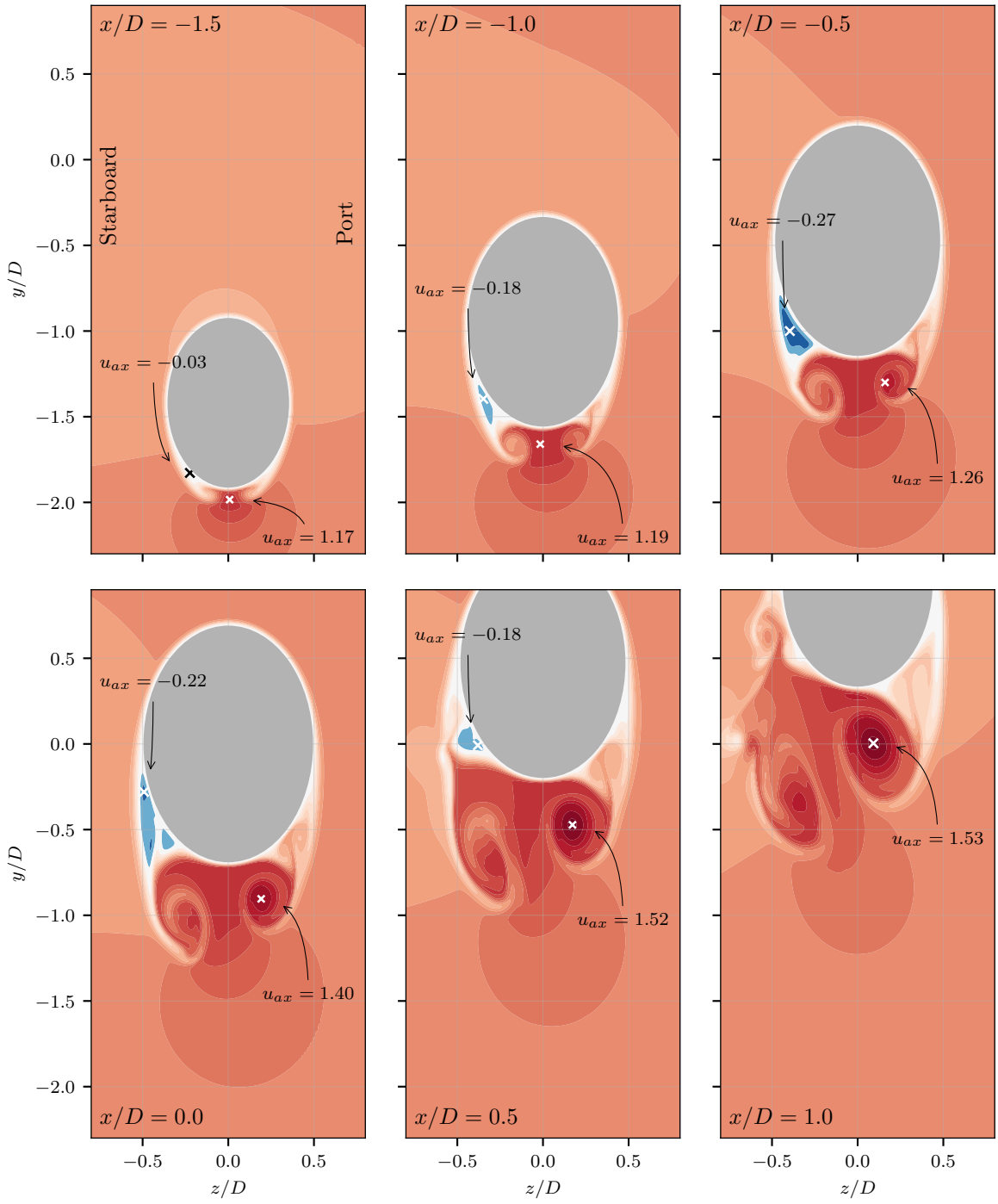

Figure 7 Axial velocity u_{ax} in the same six yz-planes along the spheroid as in figure 6. Figures are created at time $t = 345.760D/U_\infty$. The velocity component shown is the component parallel to the spheroid axis. Blue colors indicate negative and red colors indicate positive velocity. All individual plots share the same color scales. The maximum and minimum values of velocity u_{ax} are indicated on the figure with crosses.

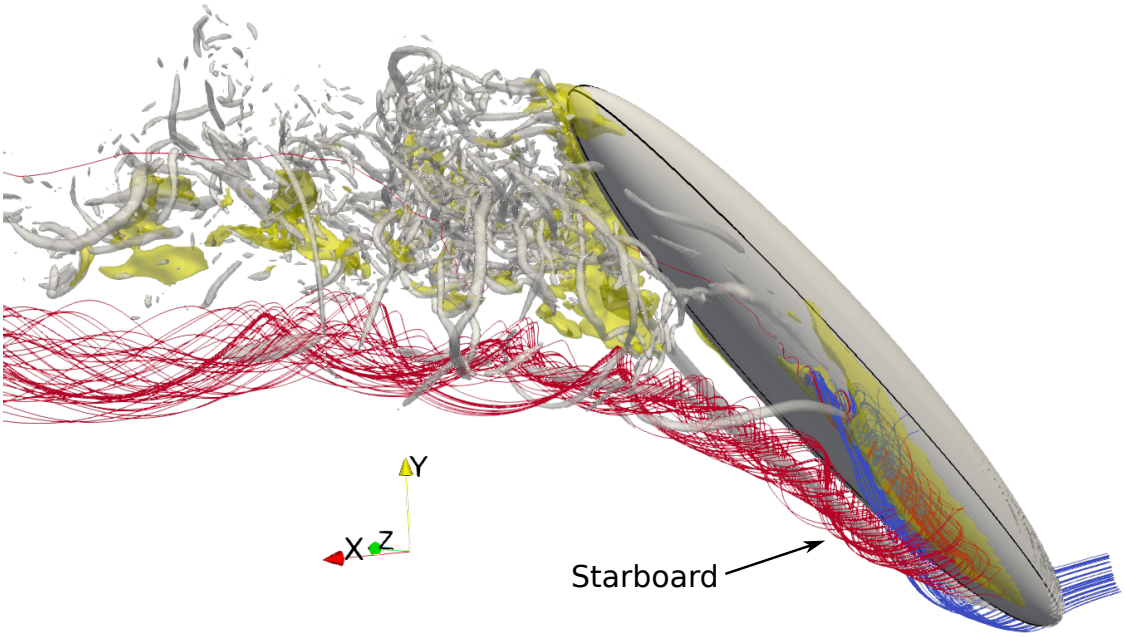

Figure 8 3-D perspective view of starboard side. Regions with backflow ($u_{ax} < 0$) are enclosed with yellow isosurfaces. The spheroid body and vortex cores (here defined by $\lambda_2 < -80$) are both grey. The streamlines are integrated from randomly selected seed points in the backflow region both upstream and downstream. The lines from the backflow region and upstream towards the inflow, are blue, and the lines exiting and moving downstream and into the wake, are red. The perimeter of the 3-D yellow region near the starboard nose is the boundary of the backflow region. Figure is created at time $t = 345.760D/U_\infty$.

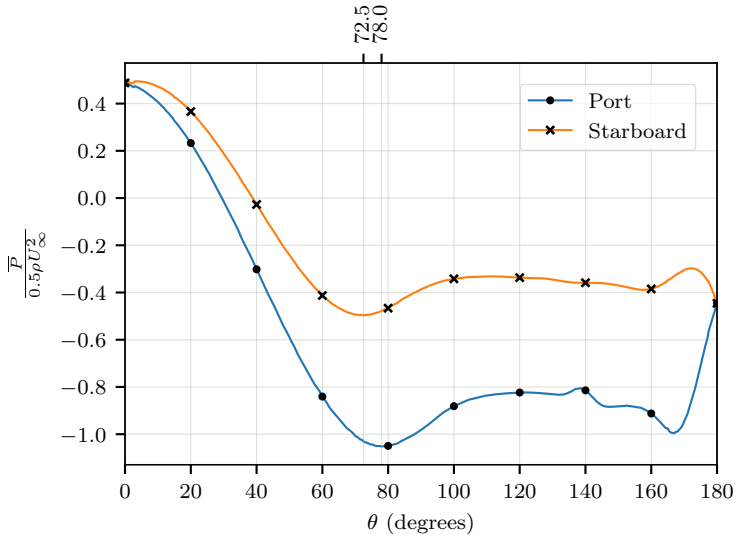

Figure 9 Time-averaged pressure along the spheroid surface at $x_{ax} = 0.0$ (the centroid of the spheroid). The minima of the pressure at port and starboard side is indicated on the upper abscissa. Zero degree is the upper ridge of the spheroid, facing the inflow, and 180 degrees are the backside of the spheroid.

less suction. The minima of the pressure is shifted downwards about five degrees on port side compared to starboard side, see figure 9. Based on observations of the flow direction a few grid cells away from the wall, we see that the flow separation at the center of the spheroid is around 90 degrees from the ridge on the starboard side and 100 degrees on the port side.

D. Interaction between the starboard main vortex and the shear layer

The weaker starboard side vortex, being deflected away from the spheroid surface and into the freestream, interacts with the double shear layers between the spheroid, backflow region and freestream. In this interaction region, a number of interesting phenomena occur. In order to explore some of them, we conducted a simulation from where we saved the entire 3-D flow field in a selected region close to the spheroid every 15th time steps, that is every $0.015D/U_\infty$. The simulation was conducted for 30 000 timesteps, which resulted in a dataset of 2000 full 3-D flow field snapshots. This collection of 3-D flow fields has been examined and interesting flow phenomena have been selected and will be discussed in the following sub-sections.

For a long duration of time a double helical structure is observed, see figure 10a). The weak starboard tip vortex interacts with a secondary vortex originating from the shear layer on the starboard side. This vortex pair curl around each other, forming a helical pair of vortices with the same rotational direction. This secondary vortex is in fact stronger (in terms of maximum vorticity in the vortex core) than the starboard tip vortex. The two vortices both rotate in the same direction, that is, they have negative axial vorticity. This is easily explained by the fact that they are both generated from the same side of the spheroid, one originating from the nose and the other originating near the center of the spheroid. The same pair of helical vortices are also shown in figure 6, in the plane at $x/D = 1.0$.

The formation of this helical pair originates from the main starboard vortex that separates from the boundary layer and turn downstream. This is particularly visible in figure 8. However, the boundary layer continues to roll up, and generates more vortices. From several time instants in the simulation we count between two and four additional vortices being generated from the starboard boundary layer. All of them have the same rotational direction, and occasionally they form helical pairs with the main starboard vortex structure.

In another sequence of repetitive events a number of delicate and almost identical hairpin vortices are formed outside of the shadow of the spheroid and shear layers, as indicated on figure 10 b) and c). The hairpin vortices are generated and elongated, while they simultaneously wrap themselves around the core of the starboard tip vortex. The origin of these hairpin vortices is the turbulence generated by the port side tip vortex when it disintegrates. At certain times, a single vortex from the port side is wrapped around the starboard side tip vortex. This is when the hairpin vortices are created.

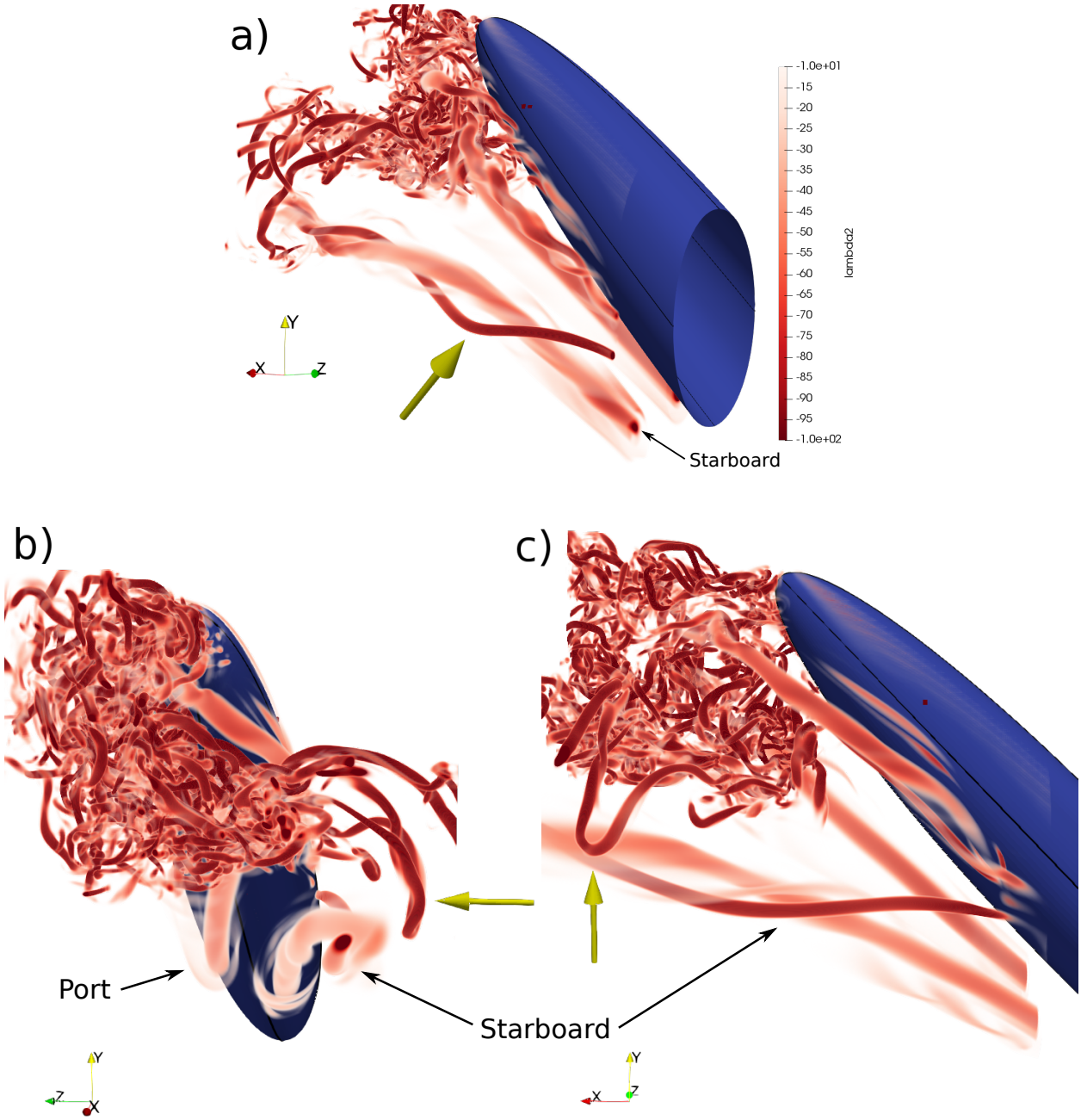

Figure 10 (a): double helical structure at time $t = 346.825D/U_\infty$. (b) and (c): hairpin vortex formation at time $t = 354.835D/U_\infty$ from two different viewpoints. The yellow arrows indicate the features of interest.

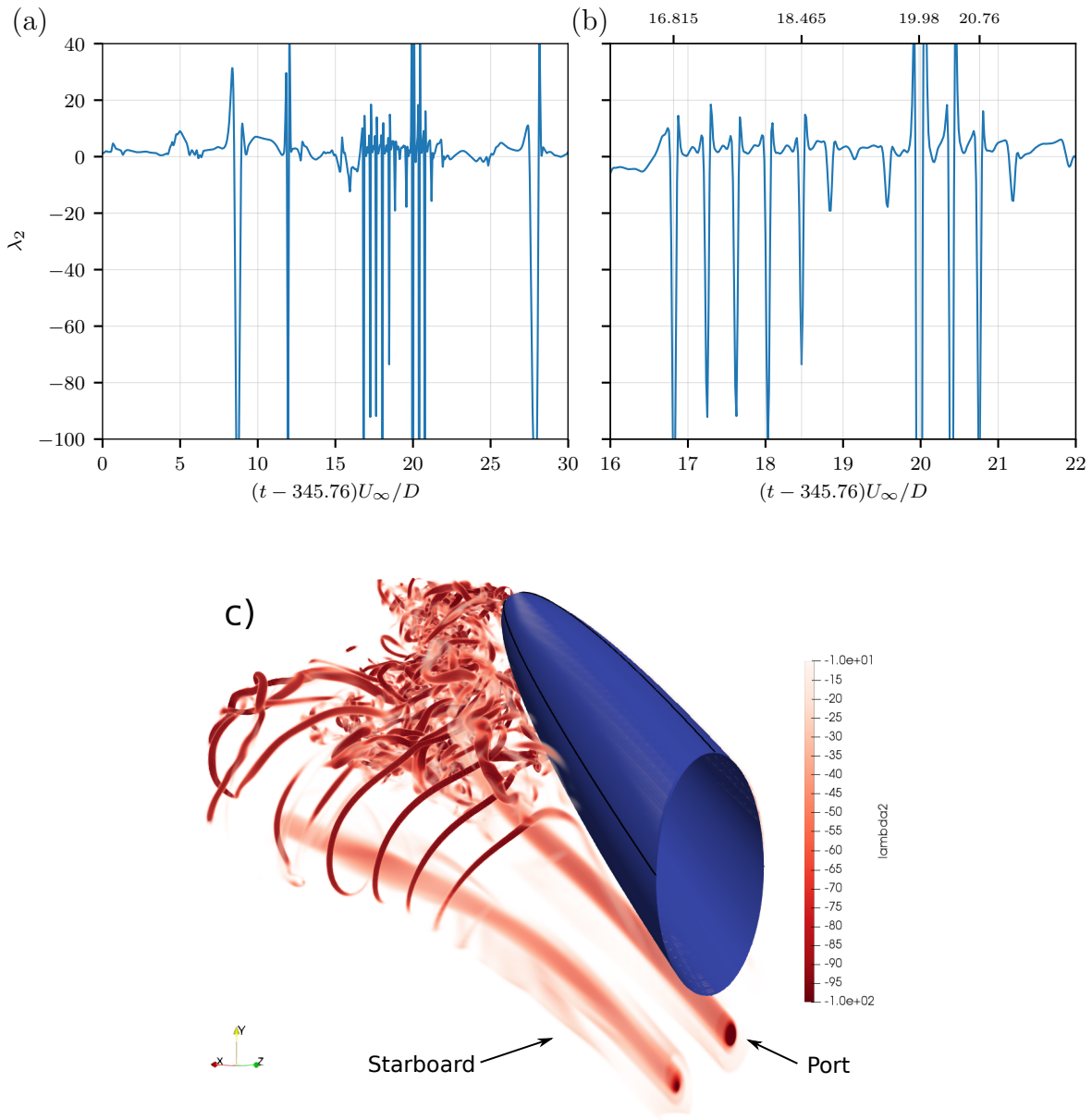

Figure 11 **a): Time-evolution of λ_2 through point $(x, y, z) = (1.5, 0.1, -0.85)$ indicating when a vortex core passes through this point. b): like a), but zoomed in around the region of the observed Kelvin-Helmholtz instabilities. c): 3-D rendering of the Kelvin-Helmholtz instability from the starboard shear layer at time $t = 363.790D/U_\infty$.**

E. Intermittent Kelvin-Helmholtz vortices

When we study the time-series from the simulations, a number of nearly identical vortex filaments are observed on the starboard side only. These are traced back to the shear layer that rolls up and forms the starboard side tip vortex. We have already discussed the double shear layers that form due to the backflow in this region, and from the outermost of these we observe the characteristic Kelvin-Helmholtz instability, similar to what occurs in the shear layer shed from a circular cylinder, see figure 11c).

Since the studied time series are limited and we only observed one of these 'bursts' of Kelvin-Helmholtz instabilities, we cannot compute the intermittency factor, but we do get a very good estimate of the frequency of these events because they occur very regularly. Figure 11 a) and b) show λ_2 in a point $(x, y, z) = (1.5, 0.1, -0.85)$ as a function of time. Each time a vortex core passes by, in the vicinity of this point, the measured value drops far below 0 in the plot. In the time intervals (16.815 - 18.465 D/U_∞ and 19.98 - 20.76 D/U_∞) we see five and three such vortices passing by. In addition there might be some vortices passing nearby in the interval 18.465 - 19.98 D/U_∞, but that is not directly clear from the plot alone. In total, from figure 11b) we can estimate the period of the instabilities to be approximately $0.4D/U_\infty$, corresponding to a frequency of 2.5 U_∞/D.

This frequency of 2.5 U_∞/D is amazingly high for a Kelvin-Helmholtz shear layer instability compared to for instance similar frequencies found in the shear layers of circular cylinders. The similar instability frequency of shear layers shedding from a circular cylinder are $5f_v$ [23], which is around $1U_\infty/D$ for a Strouhal number of 0.2. This is generally valid over a broad range of Reynolds numbers around 4000. However, there is a striking similarity between the current investigated spheroid shear layer instability and the Kelvin-Helmholtz instabilities found in shear layers around spheres. Constantinescu and Squires [24] performed direct numerical simulations on the flow around a sphere at $Re = 10000$, and found Kelvin-Helmholtz instabilities in the frequency range between 1.9 and 2.4 U_∞/D. This is in good agreement with the present result.

Another very interesting observation is that the rotational direction of the Kelvin-Helmholtz vortices are opposite of the 'intuitive direction'. In figure 12 the yellow arrows indicate regions of high and low fluid velocity, the larger arrow indicates higher velocity (details on this is shown in figure 7). Since the axial fluid velocity on the leeward side (back side) of the spheroid is *higher* than the freestream velocity, the observed Kelvin-Helmholtz vortices have a *positive* vorticity ω_y. If the fluid behind the spheroid was nearly stagnant (like the recirculation zone behind a circular cylinder) the rotation of the Kelvin-Helmholtz vortices would have been in the opposite direction.

V. Concluding Remarks

The wake behind the 45° inclined 6:1 prolate spheroid at $Re_D = 4000$ turned out to be severely skewed as in the $Re_D = 3000$ case, in spite of the completely symmetric geometry. Although the force coefficients were almost identical, the secondary torque coefficients in the present case were substantially reduced compared to the lower-Re case. Also,

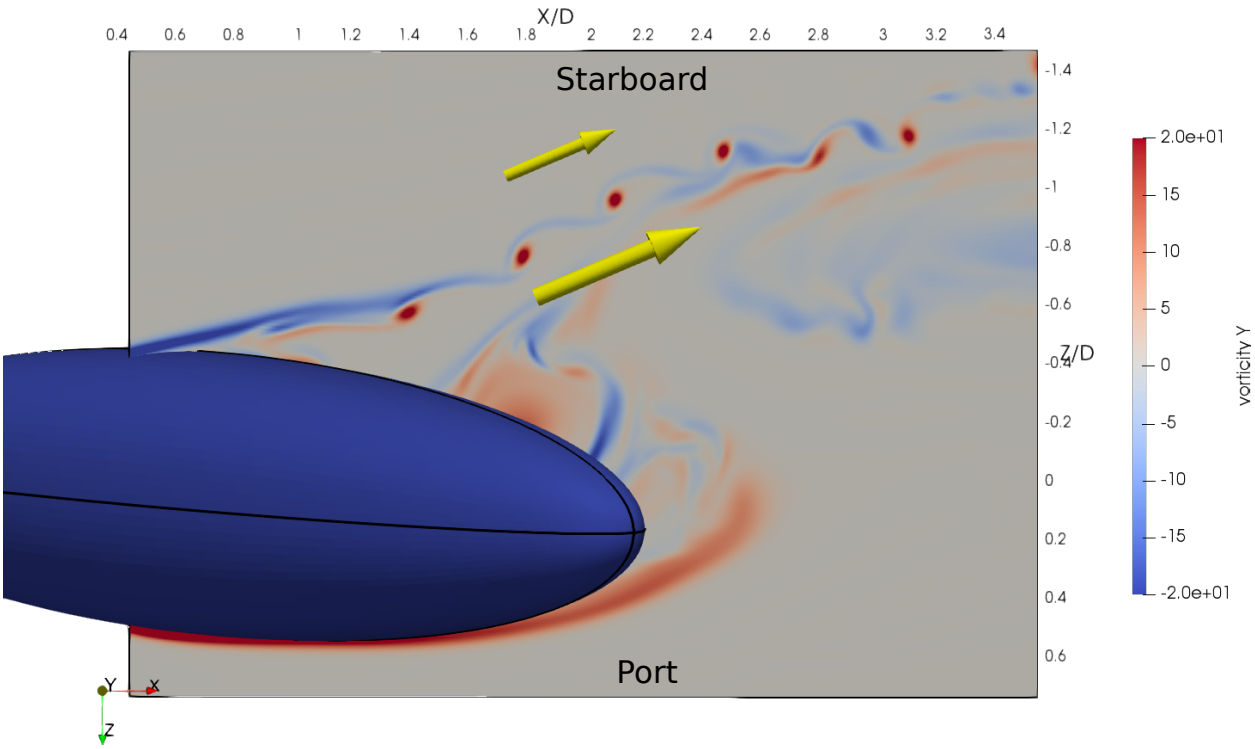

Figure 12 **A xz-slice at $z = 0.63$ colored by the vorticity ω_y, showing the Kelvin-Helmholtz vortices at time $t = 363.790D/U_\infty$. The yellow arrows indicate regions with high (large arrow) and low (small arrow) fluid velocity.**

the RMS of all force- and torque coefficients are roughly doubled from $Re_D = 3000$, which indicate a major change in the near-wake with more unsteadiness than before.

The pressure within the two main coherent vortical structures were also significantly changed from $Re_D = 3000$. The two minima from the helical vortex alteration process are almost gone in the present case. This confirms the hypothesis from the introduction, that the flow is highly transitional in this Reynolds number regime.

The present work is the first to describe the interesting backflow region associated with the weak starboard side vortex. In this region the fluid enters from behind, flows towards the nose and leave through the weak starboard side vortex. There is a continuous exchange of fluid in this region.

The interesting flow phenomena reported in section IV, namely the double helix, the hairpin vortices and the Kelvin-Helmholtz vortices, are all observed intermittently. These phenomena repeat themselves intermittently, but the accompanying animations are not sufficiently long to draw conclusions about how recurrent they are. These intermittently occurring flow phenomena are confined in space and have only negligible influence on the force coefficients shown in figure 4. The intermittent vortex dynamics in the $Re_D = 4000$ wake strongly suggest that the flow is in a transitional regime where modest variations in the Reynolds number give rise to major changes in the wake. Neither the double helix nor any Kelvin-Helmholtz vortices were observed at $Re_D = 3000$. We therefore speculate that periodic vortex dynamics phenomena may occur if the Reynolds is somewhat further increased.

We admit that the wake flow at $Re_D = 4000$ is in a transitional flow regime and strongly Reynolds number dependent. The intermittent phenomena observed herein were not reported at lower Reynolds numbers. This makes the present wake distinctly different from the wake at $Re_D = 3000$, although the overall asymmetries are in common.

VI. Acknowledgments

The authors wish to thank the employees at *KM Turbulenz GmbH* for all their help and technical support on the MGLET code. Computing time was granted by UNINETT Sigma2 under project *nn9191k*. F.J. acknowledges the funding from the Future Industry's Leading Technology Development program (No. 10042430) of MOTIE/KEIT of Korea.

References

[1] Wang, K., "Separation patterns of boundary layer over an inclined body of revolution," *AIAA Journal*, Vol. 10, No. 8, 1972, pp. 1044–1050. doi:10.2514/3.50292, URL https://dx.doi.org/10.2514/3.50292.

[2] Geissler, W., "Three-dimensional laminar boundary layer over a body of revolution at incidence and with separation," *AIAA Journal*, Vol. 12, No. 12, 1974, pp. 1743–1745. doi:10.2514/3.49593, URL https://dx.doi.org/10.2514/3.49593.

[3] Wetzel, T. G., Simpson, R. L., and Chesnakas, C. J., "Measurement of three-dimensional crossflow separation," *AIAA Journal*, Vol. 36, No. 4, 1998, pp. 557–564. doi:10.2514/2.429, URL https://dx.doi.org/10.2514/2.429.

[4] Chesnakas, C. J., Taylor, D., and Simpson, R. L., "Detailed investigation of the three-dimensional separation about a 6: 1 prolate spheroid," *AIAA journal*, Vol. 35, No. 6, 1997, pp. 990–999. doi:10.2514/2.208, URL https://dx.doi.org/10.2514/2.208.

[5] Rhee, S. H., and Hino, T., "Numerical simulation of unsteady turbulent flow around maneuvering prolate spheroid," *AIAA Journal*, Vol. 40, No. 10, 2002, pp. 2017–2026. doi:10.2514/2.1534, URL https://dx.doi.org/10.2514/2.1534.

[6] Simpson, R. L., "Aspects of turbulent boundary-layer separation," *Progress in Aerospace Sciences*, Vol. 32, No. 5, 1996, pp. 457–521. doi:10.1016/0376-0421(95)00012-7, URL https://doi.org/10.1016/0376-0421(95)00012-7.

[7] Andersson, H. I., Jiang, F., and Okulov, V. L., "Instabilities in the Wake of an Inclined Prolate Spheroid," *Computational Modelling of Bifurcations and Instabilities in Fluid Dynamics*, edited by A. Gelfgat, Springer International Publishing AG, 2018, Chap. 9, pp. 311–352.

[8] El Khoury, G. K., Andersson, H. I., and Pettersen, B., "Crossflow past a prolate spheroid at Reynolds number of 10000," *Journal of Fluid Mechanics*, Vol. 659, 2010, pp. 365–374. doi:10.1017/S0022112010003216, URL https://doi.org/10.1017/S0022112010003216.

[9] El Khoury, G. K., Andersson, H. I., and Pettersen, B., "Wakes behind a prolate spheroid in crossflow," *Journal of Fluid Mechanics*, Vol. 701, 2012, pp. 98–136. doi:10.1017/jfm.2012.135, URL https://doi.org/10.1017/jfm.2012.135.

[10] Jiang, F., Gallardo, J. P., and Andersson, H. I., "The laminar wake behind a 6:1 prolate spheroid at 45° incidence angle," *Physics of Fluids*, Vol. 26, No. 11, 2014, p. 113602. doi:10.1063/1.4902015, URL https://doi.org/10.1063/1.4902015.

[11] Jiang, F., Gallardo, J. P., Andersson, H. I., and Zhang, Z., "The transitional wake behind an inclined prolate spheroid," *Physics of Fluids*, Vol. 27, No. 9, 2015, p. 093602. doi:10.1063/1.4929764, URL https://doi.org/10.1063/1.4929764.

[12] Jiang, F., Gallardo, J. P., and Andersson, H. I., "Transition and loss of symmetry in the wake behind an inclined prolate spheroid," *8th National Conference on Computational Mechanics MekIT'15*, edited by B. Skallerud and H. I. Andersson, International Center for Numerical Methods in Engineering (CIMNE), Barcelona, Spain, 2015, pp. 219–232.

[13] Cobleigh, B., "High-angle-of-attack yawing moment asymmetry of the X-31 aircraft from flight test," *12th Applied Aerodynamics Conference*, 1994, p. 1803. doi:10.2514/6.1994-1803, URL https://doi.org/10.2514/6.1994-1803.

[14] Bridges, D., "The asymmetric vortex wake problem - Asking the right question," *36th AIAA Fluid Dynamics Conference and Exhibit*, 2006, p. 3553. doi:10.2514/6.2006-3553, URL https://doi.org/10.2514/6.2006-3553.

[15] Moskowitz, C., Dejarnette, F. R., and Hall, R. M., "Effects of nose bluntness, roughness, and surface perturbations on the asymmetric flow past slender bodies at large angles of attack," *7th Applied Aerodynamics Conference*, 1989, p. 2236. doi:10.2514/6.1989-2236, URL https://doi.org/10.2514/6.1989-2236.

[16] Ashok, A., Van Buren, T., and Smits, A., "Asymmetries in the wake of a submarine model in pitch," *Journal of Fluid Mechanics*, Vol. 774, 2015, pp. 416–442. doi:10.1017/jfm.2015.277, URL https://doi.org/10.1017/jfm.2015.277.

[17] Jiang, F., Andersson, H. I., Gallardo, J. P., and Okulov, V. L., "On the peculiar structure of a helical wake vortex behind an inclined prolate spheroid," *Journal of Fluid Mechanics*, Vol. 801, 2016, pp. 1–12. doi:10.1017/jfm.2016.428, URL https://doi.org/10.1017/jfm.2016.428.

[18] Manhart, M., Tremblay, F., and Friedrich, R., "MGLET: a parallel code for efficient DNS and LES of complex geometries," *Parallel Computational Fluid Dynamics - Trends and Applications*, edited by C. B. Jenssen, T. Kvamdal, H. I. Andersson, B. Pettersen, A. Ecer, J. Periaux, N. Satofuka, and P. Fox, Elsevier Science B.V., 2001, pp. 449–456. doi:10.1016/B978-044450673-3/50123-8, URL https://doi.org/10.1016/B978-044450673-3/50123-8.

[19] Williamson, J. H., "Low-storage Runge-Kutta schemes," *Journal of Computational Physics*, Vol. 35, No. 1, 1980, pp. 48–56. doi:10.1016/0021-9991(80)90033-9, URL http://dx.doi.org/10.1016/0021-9991(80)90033-9.

[20] Peller, N., Duc, A. L., Tremblay, F., and Manhart, M., "High-order stable interpolations for immersed boundary methods," *International Journal for Numerical Methods in Fluids*, Vol. 52, No. 11, 2006, pp. 1175–1193. doi:10.1002/fld.1227, URL http://dx.doi.org/10.1002/fld.1227.

[21] Manhart, M., "A zonal grid algorithm for DNS of turbulent boundary layers," *Computers & Fluids*, Vol. 33, No. 3, 2004, pp. 435–461. doi:10.1016/s0045-7930(03)00061-6, URL http://dx.doi.org/10.1016/S0045-7930(03)00061-6.

[22] Jeong, J., and Hussain, F., "On the identification of a vortex," *Journal of Fluid Mechanics*, Vol. 285, 1995, pp. 69–94. doi:doi.org/10.1017/S0022112095000462, URL https://doi.org/10.1017/S0022112095000462.

[23] Prasad, A., and Williamson, C. H. K., "The instability of the shear layer separating from a bluff body," *Journal of Fluid Mechanics*, Vol. 333, 1997, pp. 375–402. doi:10.1017/S0022112096004326, URL http://dx.doi.org/10.1017/S0022112096004326.

[24] Constantinescu, G., and Squires, K., "Numerical investigations of flow over a sphere in the subcritical and supercritical regimes," *Physics of fluids*, Vol. 16, No. 5, 2004, pp. 1449–1466. doi:10.1063/1.1688325, URL https://doi.org/10.1063/1.1688325.